Behavioral/Systems/Cognitive

Functional Imaging, Spatial Reconstruction, and Biophysical Analysis of a Respiratory Motor Circuit Isolated *In Vitro*

Hidehiko Koizumi,[1,2,*] Christopher G. Wilson,[1,3,4*] Stephen Wong,[1,5] Tadashi Yamanishi,[1] Naohiro Koshiya,[6] and Jeffrey C. Smith[1]

[1]Cellular and Systems Neurobiology Section, National Institute of Neurological Disorders and Stroke, National Institutes of Health, Bethesda, Maryland 20892, [2]Osaka University Graduate School of Dentistry, Osaka 565-0871, Japan, Departments of [3]Pediatrics and [4]Neurosciences, Case Western Reserve University, Cleveland, Ohio 44106, [5]Howard Hughes Medical Institute, Bethesda, Maryland 20814, and [6]Blanchette Rockefeller Neurosciences Institute, Johns Hopkins Campus, Rockville, Maryland 20850

We combined real-time calcium-based neural activity imaging with whole-cell patch-clamp recording techniques to map the spatial organization and analyze electrophysiological properties of respiratory neurons forming the circuit transmitting rhythmic drive from the pre-Bötzinger complex (pre-BötC) through premotoneurons to hypoglossal (XII) motoneurons. Inspiratory pre-BötC neurons, XII premotoneurons (preMNs), and XII motoneurons (MNs) were retrogradely labeled with Ca^{2+}-sensitive dye in neonatal rat *in vitro* brainstem slices. PreMN cell bodies were arrayed dorsomedially to pre-BötC neurons with little spatial overlap; axonal projections to MNs were ipsilateral. Inspiratory MNs were distributed in dorsal and ventral subnuclei of XII. Voltage-clamp recordings revealed that two currents, persistent sodium current (NaP) and K^+-dominated leak current (Leak), primarily contribute to preMN/MN subthreshold current–voltage relationships. NaP or Leak conductance densities in preMNs and MNs were not significantly different. We quantified preMN and MN action potential time course and spike frequency– current (*f–I*) relationships and found no significant differences in repetitive spiking dynamics, steady-state *f–I* gains, and afterpolarizing potentials. Rhythmic synaptic drive current densities were similar in preMNs and MNs. Our results indicate that, despite topographic and morphological differences, preMNs and MNs have some common intrinsic membrane, synaptic integration, and spiking properties that we postulate ensure fidelity of inspiratory drive transmission and conversion of synaptic drive into (pre)motor output. There also appears to be a common architectonic organization for some respiratory drive transmission circuits whereby many preMNs are spatially segregated from pre-BötC rhythm-generating neurons, which we hypothesize may facilitate downstream integration of convergent inputs for premotor pattern formation.

Key words: **breathing; brainstem; calcium imaging; rhythm; pre-Bötzinger complex; premotoneurons**

Introduction

Unraveling neural network function requires detailed information on architectonic and biophysical properties of different interacting neuron populations. In vertebrate rhythmic motor pattern generation networks, such as brainstem networks generating breathing or spinal networks generating locomotion, spatially distributed populations of interneurons, premotoneurons (preMNs), and motoneurons (MNs) subserve distinct functional roles. Interacting populations of interneurons generate temporal features of the motor pattern including network rhythms, preMNs (defined as cells with axonal connections to MNs) function as pattern formation elements and substrates for rhythmic drive transmission, whereas MNs generate motor output. Determining the organization of these functionally distinct populations remains a major problem in vertebrate motor circuitry (Grillner et al., 2005). Functional biophysical properties, particularly at the level of preMNs and interneurons, have also not been well established. Here, we experimentally analyze architecture and neuronal properties of a local rhythmic circuit isolated from the respiratory pattern generation network of the mammalian brainstem.

Breathing in mammals involves rhythmic activation of spinal and cranial motoneurons. Inspiratory rhythm, generated by interneurons in the pre-Bötzinger complex (pre-BötC) of the ventrolateral medulla (Smith et al., 1991; Feldman and Smith, 1995; Rekling and Feldman, 1998), propagates through preMN transmission circuits to spinal and cranial MNs. Topographical features of bulbospinal transmission circuits have been described previously (Feldman et al., 1988; Smith et al., 1991; Feldman and Smith, 1995; Ellenberger, 1999; Guyenet et al., 2002; Stornetta et al., 2003a,b), but there is less information on cranial motor transmission circuits (Dobbins and Feldman, 1995). Here, we used neural tracing and activity imaging with fluorescent Ca^{2+}-

Received Jan. 28, 2007; revised Jan. 11, 2008; accepted Jan. 13, 2008.

This work was supported by the Intramural Research Program of the National Institute of Neurological Disorders and Stroke, National Institutes of Health. We thank George Dold and David Ide for technical support and Joyce Hairston, Dianna Brewer, and Ruli Zhang for assistance with histology and confocal imaging.

*H.K. and C.G.W. contributed equally to this work.

Correspondence should be addressed to Dr. Jeffrey C. Smith, Porter Neuroscience Research Center, Building 35, Room 3C-917, 35 Convent Drive, National Institute of Neurological Disorders and Stroke, National Institutes of Health, Bethesda, MD 20892. E-mail: jsmith@helix.nih.gov.

S. Wong's present address: Department of Neurology, Hospital of the University of Pennsylvania, Philadelphia, PA 19104.

DOI:10.1523/JNEUROSCI.3553-07.2008

 0270-6474/08/282353-13$15.00/0

sensitive dyes in conjunction with high-resolution structural imaging (Koshiya and Smith, 1999) to map inspiratory hypoglossal (XII) preMNs and MNs in the circuit transmitting rhythmic inspiratory drive from the pre-BötC to musculature of the tongue. To accomplish this, we exploited neonatal rat medullary slice preparations, which are used for analysis of inspiratory rhythm and pattern generation mechanisms (Smith et al., 1991; Koshiya and Smith, 1999; Del Negro et al., 2001). These slices contain active rhythm-generating pre-BötC neurons and circuits transmitting rhythmic inspiratory drive to XII MNs. By combining our imaging approach with electrophysiological analyses, we reconstructed novel biophysical and topological features of this circuit.

Our reconstruction suggests an architectonic organization whereby many XII preMNs are spatially segregated from pre-BötC rhythm-generating neurons, an arrangement that has also been found for bulbospinal circuits *in vivo* and may facilitate downstream integration of convergent inputs for premotor pattern formation. Our analysis also indicates that preMNs and MNs share a similar set of synaptic and intrinsic electrophysiological properties, which we hypothesize represents a common electrophysiological foundation for neurons functioning as rhythmic drive transmission elements. We also compare some of these properties to those of pre-BötC interneurons, extending our analysis to include specialization endowing a subset of pre-BötC neurons with unique rhythmogenic properties within the circuit.

Materials and Methods

Slice preparations. We cut transverse slices (280–350 μm thick) of medulla oblongata from Sprague Dawley neonatal [postnatal day 0 (P0) to P4] rats as previously described (Koshiya and Smith, 1999) to contain the pre-Bötzinger complex and rostral end of the XII motor nucleus with XII nerve rootlets. The slice was mounted in a recording chamber (0.2 ml) on a microscope stage and superfused (4 ml/min) with artificial CSF (ACSF) containing the following (in mM): 124 NaCl, 25 $NaHCO_3$, 3 KCl, 1.5 $CaCl_2 \cdot 2H_2O$, 1.0 $MgSO_4 \cdot 7H_2O$, 0.5 $NaH_2PO_4 \cdot H_2O$, 30 D-glucose, and antibiotics (500 U/L penicillin, 0.5 mg/L streptomycin, and 1 mg/L neomycin), equilibrated with 95% O_2 and 5% CO_2 (pH 7.35–7.40 at 27 ± 1°C). Rhythmic respiratory network activity in the XII nerves was maintained for up to 36 h by elevating the superfusate K^+ concentration to 8–9 mM.

Neuronal labeling and imaging. Methods for labeling pre-BötC neurons with Ca^{2+}-sensitive dye based on their axonal projections and for imaging Ca^{2+}-sensitive dye fluorescence activity as a monitor of population and single-cell rhythmic activity have been described previously (Koshiya and Smith, 1999). A similar approach involving retrograde labeling of neurons, which we call "functional neural tracing," was used here to label XII preMNs and MNs. Our population labeling approach, based on axonal projections and network connectivity, and using acetoxymethyl (AM) forms of Ca^{2+}-sensitive dyes, is an extension of the methods originally described by O'Donovan et al. (1994) and Fetcho and O'Malley (1995) for retrograde labeling of neurons in brainstem–spinal cord motor circuits with Ca^{2+}-sensitive dyes. Our use of a membrane-permeant AM ester form of dye enabled us to retrogradely label neurons with Ca^{2+}-sensitive dye through axons of passage without affecting axonal or network function (Koshiya and Smith, 1999). Briefly, the membrane-permeant Ca^{2+}-sensitive dye, Calcium Green-1 AM (CaG) (50 μg; Invitrogen, Eugene, OR), dissolved in 5 μl of DMSO containing 25 μg of pluronic F-127 (BASF, Florham, NJ) and dispersed in 10 μl of ACSF, was microinjected with a glass pipette (~10–15 μm tip diameter) in separate slices into either (1) the slice midline to bilaterally and retrogradely label somata of a subset of pre-BötC neurons, (2) the XII motor nucleus in the slice to retrogradely label a subset of XII preMNs overnight (10–16 h), or (3) into the XII nerve axon bundle in the slice to retrogradely label a subset of MNs (6–8 h). In some experiments, we alternatively applied Calcium Green-1 Dextran (10,000 molecular weight) to the XII nerve rootlet through a suction pipette for retrograde MN labeling. In addition, in some preMN labeling experiments, we injected CaG along the ventrolateral margins of the XII motor nucleus so that the dye was also distributed immediately outside of the zone of MN somata; this allowed for dye uptake by axons passing into the nucleus as well as by axons with local terminations in MN dendritic fields that extend outside the nucleus of cell somata (see Figs. 5, 6). In all experiments, we made multiple overlapping injections of dye at different depths within the tissue to allow for dye uptake by as many axons as possible that project through/into the region. For a given injection site, both rhythmically active and nonrhythmically active neurons were labeled in variable proportions; these latter neurons were not components of the respiratory network and accordingly were not studied. Our use of real-time fluorescence background subtraction (below) allowed us to readily identify and focus exclusively on the rhythmically active cells.

We visualized CaG-labeled inspiratory neurons in multiple focal and image planes with a fixed-stage upright videomicroscope (Axioskop-FS1; Zeiss, Thornwood, NY) with appropriate optical filters (excitation, 485 nm, emission, 530 nm; 505 nm beam splitter; standard FITC cube; Omega Optical, Brattleboro, VT) and water-immersion objectives (Zeiss Achroplan). Incident illumination intensities (via neutral density filters) were typically 0.3–1.0% of source (xenon lamp) intensity to avoid photobleaching. Fluorescence images were captured (30 frames/s) with a CCD camera fiber-optically coupled to an image-intensifier (ICCD-1000F with luminous gain of 80,000; Videoscope International, Sterling, VA) and recorded on videotape simultaneously with electrophysiological signals, allowing temporal locking and reconstruction of optical signals in relationship to electrophysiological signals. Changes in fluorescence intensity ($\Delta F/F$) were detected in real time with an image processor (ARGUS 20; Hamamatsu Photonics, Bridgewater, NJ) and quantified off-line after digitizing images using an analog to digital converter (DVMC-DA2 media converter; Sony, Tokyo, Japan). Output resolution of the CCD camera, which incorporated a full frame transfer array, was >700 TV lines/picture height horizontal (H) by 486 TV lines vertical (V), and our digitized image resolution was 640 (H) by 480 (V) pixels. This resolution provided submicrometer- and micrometer-level spatial resolutions at optical magnifications of 63 and 20×, respectively (Koshiya and Smith, 1999), as verified by image calibration. Processing of fluorescence signals off-line with Savitzky-Golay filters implemented in Igor Pro software (WaveMetrics, Lake Oswego, OR) was used to improve signal-to-noise when fluorescence transients were small (<10% changes from baseline fluorescence). Inspiratory "flash" images, used to analyze and display snapshots of peak fluorescence activity, were obtained by subtracting the baseline CaG images from images acquired during peak inspiratory activity in real time (using the ARGUS 20) and applying 8-bit pseudocoloring. In some cases, we also used moving averages (typically eight frames) of optical signals to reduce background photon stochastic noise.

We simultaneously obtained videomicroscopic infrared (IR)–differential interference contrast (DIC) images (Dödt and Zieglgänsberger, 1994) for structural visualization with an extended IR Newvicon camera (Hamamatsu Photonics). Images were enhanced with the ARGUS 20 in real time. Infrared (900 nm) transmission was optimized with a polarizer (wide spectrum; Melles Griot, Rochester, NY) and analyzer (850–950 nm; Polarcor, Corning, NY). For simultaneous imaging, both the Newvicon and ICCD cameras were mounted on a dual-port imaging head incorporating a dichroic beam splitter (700 nm; Zeiss), and images were aligned by scan range shifting of the Newvicon camera to match the dimensions of the ICCD-1000F visual field (Foskett, 1988).

In a typical experiment, we first identified the main loci of rhythmic population florescence activity at 20× magnification, and then we used higher-magnification (40 and 63×) imaging to identify individual rhythmically active neurons within these regions of interest. For morphological reconstruction of the locations of the CaG-labeled inspiratory neurons, we obtained these high- and medium-magnification images, respectively, of individual labeled neurons and regional CaG fluorescence for each neuron population along with IR-DIC structural images obtained at these and lower (5×) magnifications for each slice recorded from. This allowed us to (1) overlay IR-DIC structural and fluorescence

images at multiple levels of structural resolution (see Figs. 1, 3), and then (2) produce composite maps of population and individual neuron locations (see Fig. 4) from different slices by aligning IR-DIC images according to structural landmarks with fluorescence images superimposed.

For some cells, we used biocytin (1–2%) (Horikawa and Armstrong, 1988) in the pipette solution to stain the cells for later histological verification of neuronal locations as well as for reconstruction of somatodendritic architecture and axonal projections. The slices were immersion fixed in 4% paraformaldehyde, 0.1 M PBS solution for 24 h at 4°C. For visualization of biocytin, the tissue was treated with 0.05% diaminobenzidine tetrahydrochloride as a chromagen. Reconstructions were performed with stained cells in whole-mounted slices visualized by light microscopy (for single-cell morphological analyses and at longer length scales for axonal projection reconstructions). For some slices, we also used confocal imaging for high-resolution reconstruction of cell morphology. These slices were cryoprotected overnight at 4°C in 30% sucrose, 0.1 M PBS solution and sectioned coronally (50 μm) on a freezing microtome. Floating sections were rinsed with PBS and incubated for 2 h at room temperature with 1:500 Texas Red Avidin D (Vector Laboratories, Burlingame, CA) to label biocytin-filled cells. Sections were mounted on slides and covered with an anti-fading medium (Prolong Gold; Invitrogen). Confocal images of Texas Red-labeled neurons were obtained with a laser-scanning imaging system (Zeiss LSM 510). Stacks of images containing multiple optical sections were acquired and analyzed to document cell morphological features. Image reconstructions were produced with Zeiss LSM 510 software and Volocity imaging software (Improvision, Lexington, MA). To reconstruct axonal projections throughout the entire slice (see Figs. 6, 7), we acquired photomicrographic images of biocytin-filled neurons at multiple focal planes in relevant regions of the slice. We then digitally merged the layered images (with Adobe Photoshop 7.0) into a master two-dimensional projection image, which allowed us to reconstruct somatodendritic morphology and axonal projection patterns.

Electrophysiological recording and analysis. We recorded extracellular XII activity with fire-polished glass suction electrodes, amplified 50,000–100,000× (CyberAmp 380; Molecular Devices, Union City, CA), bandpass filtered (0.3–2 kHz), digitized (10 kHz), and then full-wave rectified and averaged over a 30–100 ms window ($\int$XII) by either an analog Paynter filter (Bak Instruments, Rockville, MD) or digitally with Chart software (ADInstruments, Colorado Springs, CO). We recorded whole-cell voltage- and current-clamp data from the optically identified inspiratory neurons (Koshiya and Smith, 1999) imaged at high resolution (63×); these neurons were at depths in the slice up to the limits of single-cell Ca^{2+} dye fluorescence and IR-DIC optical resolution (~80 μm). In some experiments, we also obtained current-clamp recording from non-imaged pre-BötC neurons via "blind" whole-cell patch-clamp recording (Smith et al., 1991), in which electrodes were advanced into the center of the imaged pre-BötC at depths in the slice up to 150 μm; this enabled us to also stain identified inspiratory neurons with biocytin and reconstruct the morphology of pre-BötC neurons located deeper in the slice than those accessible by combined Ca^{2+} fluorescence and IR-DIC imaging. Recordings were obtained with a HEKA EPC-9 (version C) or EPC-10 amplifier (HEKA Elektronik, Southboro, MA) or an Axopatch-1D amplifier (Molecular Devices) controlled by Pulse software (HEKA; 2 kHz low-pass filter on Axopatch 1D and 2.9 kHz on HEKA amplifiers). The recording electrodes (4–6 MΩ) were positioned with microdrives (Narishige, Tokyo, Japan; SD Instruments, San Diego, CA). The pipette solution contained the following (in mM): 130.0 K-gluconate, 10.0 Na-gluconate, 4.0 NaCl, 10.0 HEPES, 4.0 Mg-ATP, 0.3 Na-GTP, and 4.0 sodium phosphocreatine, pH 7.3. Measured potentials were corrected for the liquid junction potential (−10 mV).

For analysis of intrinsic membrane and electrophysiological properties, the excitatory synaptic transmission critical for respiratory network function *in vitro* was blocked using the non-NMDA glutamate receptor blocker, 6-cyano-7-nitroquinoxaline-2,3-dione disodium (CNQX) (Sigma, 20 μM), or calcium channel blocker, Cd^{2+} (200 μM; Sigma, St. Louis, MO). We also analyzed voltage dependence and kinetics of whole-cell currents from voltage-clamp data using Pulsefit (HEKA), Chart (AD Instruments, Colorado Springs, CO), and Igor Pro software. We used a slow voltage-ramp protocol (30 mV/s; −100 to +10 mV) to prevent activation of the transient fast action potential-generating Na^+ current, while allowing us to measure slowly inactivating currents [e.g., persistent sodium current (NaP)] in inspiratory neurons (Del Negro et al., 2002). Cell capacitance (C_m) was determined from the integral of the transient capacity current (I_C, leak subtracted) evoked by a 15 ms hyperpolarizing voltage-step commands applied within −10 mV of resting potential, using $\int I_C dt = -Q_m$ at each command potential (V_m). C_m was determined from the slope of the plot of Q_m versus ΔV_m for the series of step commands. Series resistance (R_S) was calculated from the decay-time constant of I_C. Neurons failing to meet the criterion $R_m > 10\ R_S$ necessary to achieve space clamp were excluded from voltage-clamp analysis. Furthermore, neurons with clear evidence of poor space clamp such as unclamped action potentials were omitted from the analysis. We also applied analog R_S compensation ($\leq$ 80%) to assure stationary voltage-clamp conditions. Tetrodotoxin (TTX) (Sigma) was dissolved in the bathing solution to obtain a 1 μM final bath concentration for complete sodium current blockade and applied to the slice to extract TTX-sensitive NaP. Voltage-ramp data were fitted to Boltzmann functions: $g/g_{max} = [1 + \exp([V_m - V_{1/2max}]/k)]^{-1}$, where g and g_{max} represent whole-cell conductance at V_m and the maximal conductance, respectively; V_m is membrane potential; $V_{1/2max}$ is the voltage for half-maximal activation; and k is a slope factor. Statistical significance was determined by a Student's paired t test on mean data, and data are presented as means ± SD unless otherwise indicated.

In some experiments, we injected depolarizing current pulses (2 ms; 0.5–1.2 nA) under current clamp to evoke action potentials in XII preMNs or MNs and examine the time courses of the action potential (AP), fast and medium afterhyperpolarizations (fAHP and mAHP, respectively), and afterdepolarizations (ADPs). The mAHP duration (average of 10 or more evoked APs) was measured from a point with a voltage equal to baseline V_m immediately after the action potential to the point at which the voltage once again equaled this V_m. We also evoked repetitive spiking in preMNs or MNs by a series of sustained current pulses (2 s duration) of increasing amplitude, and we analyzed the instantaneous frequency of AP discharge, steady-state firing frequency, and spike frequency accommodation.

Results

Activity imaging and spatial mapping of inspiratory XII preMNs, MNs, and pre-BötC neurons

We imaged CaG fluorescence in real time in inspiratory pre-BötC neurons, XII preMNs, and MNs at macroscopic (population) and single-cell resolutions to reconstruct spatial distributions and allow targeting of neurons for electrophysiological analysis. Individual CaG fluorescent-labeled neurons in each population were also imaged structurally with IR-DIC optics for whole-cell electrophysiological recording, which also allowed neuronal staining for morphological reconstruction. Spatial distributions of the different populations of rhythmically active cells identified from the Ca^{2+} imaging, considered in detail in this section, are summarized in Figures 1–4 and morphological features of the pre-BötC–preMN–MN circuit are shown in Figures 5–8. Single-cell imaging was limited to relatively superficial cells in the slice even with IR-DIC (up to ~80 μm deep for all populations) (see Materials and Methods), whereas our population-level imaging includes scattered light from deeper neurons labeled with our technique (Koshiya and Smith, 1999). Both approaches produced essentially superimposable maps (see Fig. 4). Thus, we conclude that our activity maps are representative of the distributions of rhythmically active neurons within the slice.

XII preMNs

Microinjection of CaG into the XII motor nucleus resulted in retrograde fluorescent labeling of reticular formation XII preMNs ($n = 40$ slices). In all experiments, a subpopulation (Fig. 1*A*, circled region) of these labeled neurons exhibited increased

fluorescence intensity ($\Delta F/F$) (Fig. 1*B*) during the inspiratory phase of network activity as monitored by hypoglossal nerve discharge ($\int$XII). Retrograde labeling of this rhythmically active cell population, which represents inspiratory neurons whose axons are within the confines of the slice, was strictly ipsilateral. We analyzed Ca^{2+} dynamics in individual neurons at 63× magnification (Fig. 1*A*, inset; *C*) and identified labeled neurons as inspiratory cells by visualizing intracellular somatic Ca^{2+} transients in real time and determining whether the Ca^{2+} signal was synchronous with XII motor discharge. Figure 1*C* shows $\Delta F/F$ for four simultaneously imaged cells out of the labeled population from a typical experiment. The onset times of CaG fluorescence transients in the preMNs varied between neurons and fluctuated from cycle to cycle in a given neuron, but in general, onset times bracketed (50 ms before and after) the onset of inspiratory XII motor discharge; the duration of the fluorescence signal was typically longer (600–800 ms decay time constant) than the period of electrophysiologically recorded motor nerve activity (Fig. 1*C*), reflecting the kinetics of intracellular Ca^{2+} buffering and sequestration.

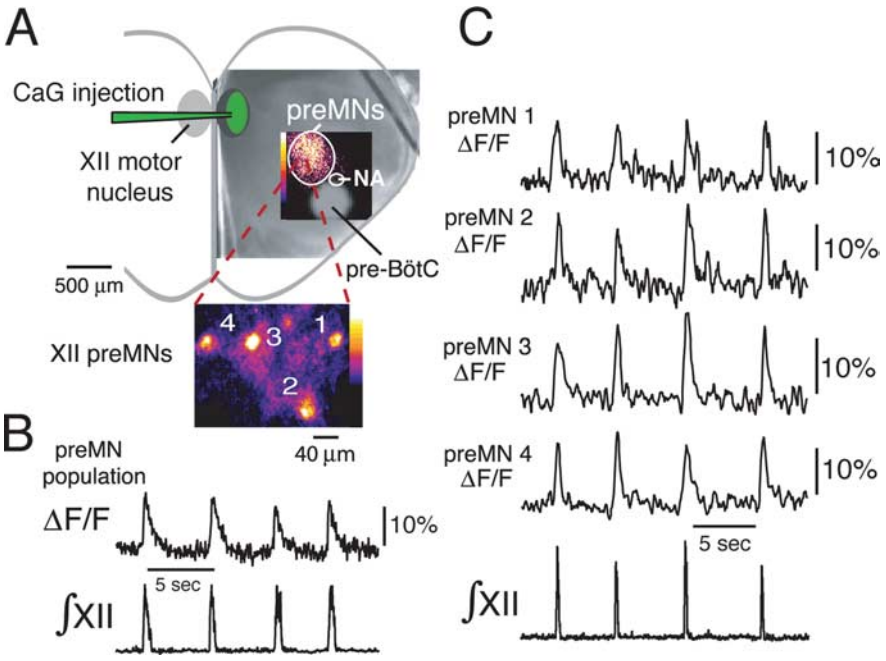

Figure 1. Functional imaging of inspiratory XII premotoneurons. ***A***, CaG injection site within the XII motor nucleus and localized inspiratory-related CaG fluorescence "flash" image (pseudocolored, background-subtracted) during peak inspiratory activity of the region where XII preMNs are located dorsomedial to the semicompact division of nucleus ambiguous (NA) and pre-BötC. The CaG fluorescence image is superimposed on a low-power (5×) IR-DIC image of the *in vitro* slice. The inset shows a high-magnification (63×) image (background-subtracted, pseudocolored) from within the circular region, showing cell bodies of individual (numbered) inspiratory neurons imaged simultaneously in the same focal plane. ***B***, Rhythmic increases in CaG fluorescence ($\Delta F/F$) in the circular area indicated in ***A*** showing regional preMN population activity-related fluorescence (20× magnification) synchronous with integrated inspiratory XII motoneuron population discharge ($\int$XII). ***C***, Fluorescence intensity signals versus time for the four preMNs shown in the high-magnification inset in ***A***, indicating rhythmic changes in $\Delta F/F$ in phase with $\int$XII.

We obtained supporting evidence that these labeled neurons were preMNs with axonal projections to the XII motor nucleus by the following: (1) confirming that short-duration activation with focal electrical stimulation (bipolar electrode, 1–2 Hz, < 100 μA) of the XII motor nucleus produced transients in the population fluorescence signal, whereas longer stimuli evoked a sustained $\Delta F/F$ signal ($n = 4$ slices) (Fig. 2*A*) (for location of XII motor nucleus in relation to preMNs, see Fig. 1); (2) establishing that this stimulation of the XII motor nucleus evoked cellular fluorescence transients in single imaged neurons ($n = 6$) (Fig. 2*B*), consistent with antidromic stimulation of neurons; (3) verifying that we could evoke action potentials in the neurons with characteristic invariant short latency during whole-cell recording, also consistent with antidromic neuronal stimulation (Fig. 2*C*); and (4) filling individual cells with biocytin and histologically verifying axonal projections within the motor nucleus ($n = 12$ neurons) (see Fig. 6).

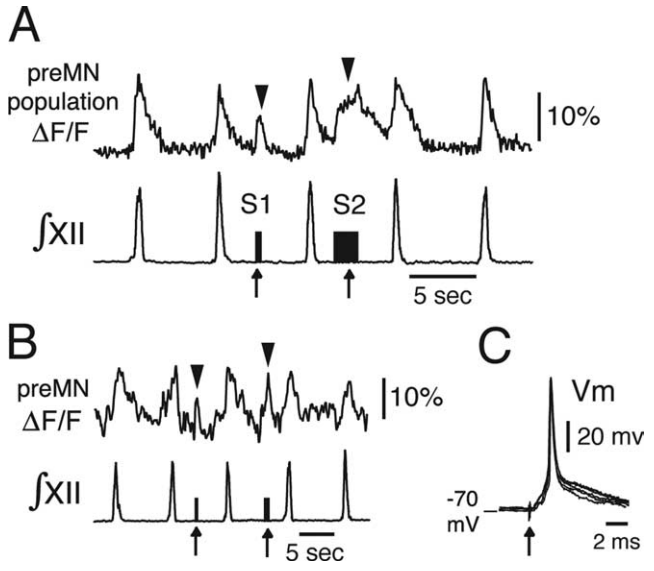

Figure 2. Antidromic activation of XII preMNs electrophysiologically confirming axonal projections of imaged preMNs to the XII motor nucleus. ***A***, Regional population CaG fluorescence transients ($\Delta F/F$) produced by focal electrical stimulation of the ipsilateral XII motor nucleus (1–2 Hz; 60 μA). Durations of the stimulation epochs are given by the stimulus artifacts (S1 and S2, arrows) in the $\int$XII trace obtained from recordings of XII MN population activity in the contralateral XII nerve root. With short antidromic stimulus epoch (S1), there is a correspondingly short duration fluorescence transient (arrowhead), whereas the transient is proportionately longer and of higher amplitude with a longer stimulus epoch (S2). ***B***, Single-cell fluorescence transients were evoked (arrowheads) in individual preMNs with similar stimulus parameters to those evoking population responses. ***C***, Individual short-latency spikes (V_m; current-clamp recordings) evoked in an imaged preMN by single antidromic stimulus pulses (10 ms duration; 5 evoked spikes superimposed) during whole-cell recording.

XII MNs

To retrogradely label XII MNs, we either microinjected CaG along the axon tract of the XII motor nerve ($n = 6$ slices) or loaded cells with CaG-dextran ($n = 16$ slices) through a suction electrode applied to the cut end of the XII nerve root (Fig. 3*A*). With either approach, in a given slice, we imaged activity of the labeled MNs with rhythmic changes in Ca^{2+} fluorescence intensity during the inspiratory phase. Examples of simultaneously imaged inspiratory MNs are shown in Figure 3, *B* and *C*.

Pre-BötC neurons

Microinjection of CaG into the midline of the slice dorsal to the inferior olivary nucleus resulted in bilateral labeling of a rhythmically active population of pre-BötC neurons, as we previously

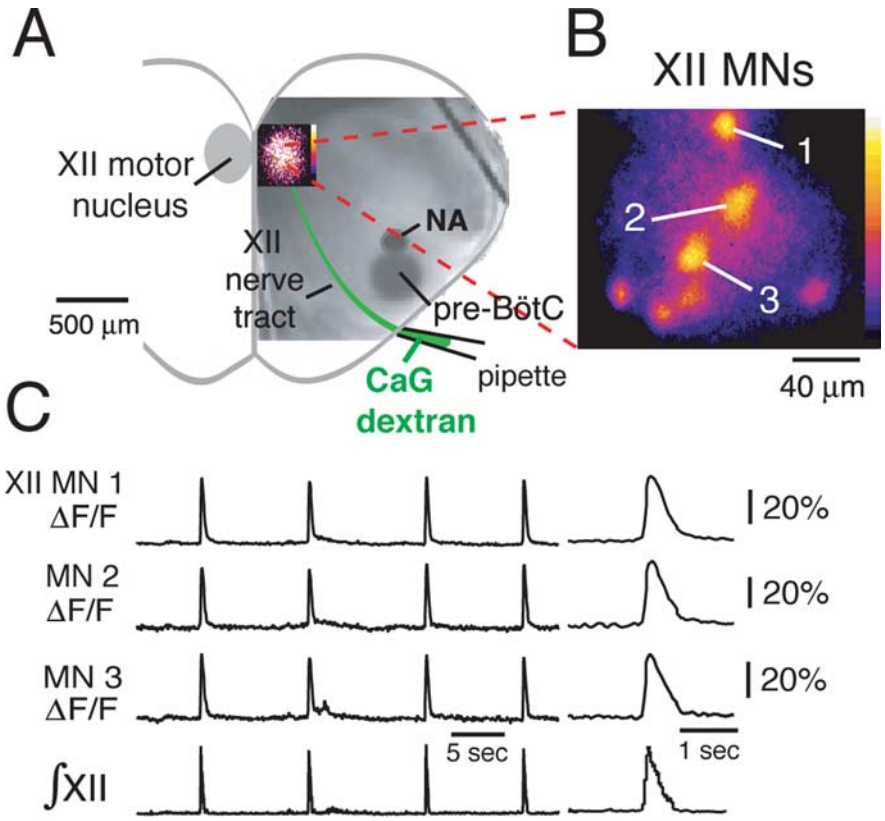

Figure 3. Functional imaging of CaG-labeled inspiratory XII motoneurons. ***A***, Rhythmically active XII MNs were labeled retrogradely by CaG-dextran loaded over 6–8 h through a suction electrode applied to the cut end of the rostralmost XII nerve root. Localized inspiratory population CaG fluorescence "flash" image in the XII motor nucleus is shown superimposed on IR-DIC image of the slice. ***B***, High-magnification (63× composite), background-subtracted, and pseudocolored flash image shows individual inspiratory MNs imaged simultaneously (7 neurons shown) in a single focal plane. ***C***, Rhythmic elevations in CaG fluorescence ($\Delta F/F$) in three inspiratory MNs (neuron somata labeled 1–3 in ***B***) in phase with inspiratory XII nerve discharge ($\int$XII); expanded time base of CaG fluorescence transients during inspiratory burst are shown at right. NA, Semicompact division of nucleus ambiguus.

described (Koshiya and Smith, 1999), which represents a subset of the total population of rhythmically active cells in this region (see Discussion). The distribution of active pre-BötC neurons from population-level imaging is shown in Figure 4. The time course of Ca^{2+} transients in single rhythmically active pre-BötC neurons (data not shown) was similar to those described previously (Koshiya and Smith, 1999); the single-cell resolution analysis presented here focused on morphological reconstruction of functionally identified, labeled cells. Examples of pre-BötC neuron morphology and such reconstructions are shown in Figures 5–8 (below).

Composite maps of inspiratory neuron populations and single neuron morphological characteristics

A composite topographical map showing the locations of imaged rhythmically active XII preMNs ($n = 146$ neurons from 40 slices) and MNs (90 identified in 22 slices total; $n = 42$ from eight slices shown) in spatial relationship to the main locus of functionally imaged pre-BötC activity is shown in Figure 4. At the level of the slice, preMNs were confined to a region ~400 μm in diameter within the plane of the slice, which corresponded closely to the locus of population activity imaged at lower magnification (20×). This preMN locus was primarily arrayed dorsomedial to nucleus ambiguus (NA) with little spatial overlap of the pre-BötC as defined by the population activity imaging. Approximately 7% of the inspiratory preMNs identified (10 of 146) were found in the pre-BötC. In additional preMN labeling experiments ($n = 15$ slices) in which we injected dye into the margin of the XII motor nucleus for dye uptake by incoming axons or locally terminating axons (see Materials and Methods), we found a similar spatial distribution of preMNs using this labeling technique. Inspiratory XII MNs were distributed throughout dorsal and ventral subregions of the motor nucleus, with slightly more of the neurons (57% of 90 cells) distributed in ventral subnuclei.

Examples of *in situ* morphology of pre-BötC neurons, preMNs, and MNs are shown from photomicrographs in Figure 5, which indicate somatic locations and features of somatodendritic morphology for several inspiratory cells labeled individually. More detailed reconstructions of somatodendritic morphology and axonal projections are shown in Figures 6–8, which illustrate structural features relating to cell and network architecture derived from reconstructions of the different cell types. These reconstructions do not represent the full three-dimensional distribution of dendritic fields or axon collateral projections as they exist in the intact brainstem because many dendrites and axon collaterals are likely cut at the slice surface. Our primary objective for the morphological reconstructions was to determine features of somatodendritic morphology and axonal projection patterns relevant to the function and pathway of the circuit isolated within our *in vitro* slices.

Pre-BötC neurons

Pre-BötC inspiratory neurons exhibited intrinsic bursting and nonintrinsically bursting electrophysiological behavior when non-NMDA glutamatergic synaptic transmission is blocked with CNQX (Koshiya and Smith, 1999; Del Negro et al., 2002). We examined morphologies of both types of cells. All of these reconstructed neurons ($n = 25$ total, 10 intrinsic bursters, 15 nonintrinsic bursters) has axonal projections into the region of the contralateral pre-BötC (as defined by activity imaging). Axons were identified as smaller diameter processes that typically arose proximally from a large-diameter primary dendrite and that could be traced for distances >500 μm beyond the dendritic field. Axons of many ($n = 17$ of 25) of the labeled pre-BötC neurons projected first through the ipsilateral preMN area (Figs. 6, 7), making a hairpin turn through this area en route to the midline, and had locally branching collaterals in the preMN zone; these collaterals were identified as smaller diameter branches from the main stem axon with fine arborizations that in some cases had punctate endings. Axons of the other reconstructed cells coursed more ventrally before crossing the midline (Fig. 6). In all cases, the axons crossed the midline through the nucleus raphé obscurus. Dendritic arborizations of all cells extended outside of the zone of pre-BötC neuron somata as mapped by the CaG fluorescence imaging. The majority of the neurons (23 of 25) had ventral dendritic arborizations extending close to the

marginal zone (within 90 μm) of the ventral medullary surface (Fig. 6). All of these neurons were multipolar cells with three to five primary dendrites with variations in soma shapes and size (maximal diameters of 15–20 μm) (see Figs. 5, 8). Many of these cells (18 of 25) exhibited prominent spines (see also Fig. 8*C*,*D*) on proximal dendrites. We did not find prominent or consistent differences between inspiratory neurons with intrinsic bursting versus nonintrinsic bursting properties in terms of soma shapes/size, primary dendrite branching patterns, occurrence of dendritic spines, or axonal projection patterns (except for preMNs in the pre-BötC, below). We found evidence of collateral innervation with axonal arborizations in the area of nucleus ambiguus motoneuron semicompact formation for some of these cells ($n = 10$).

To determine whether the axonal projection patterns and morphological features obtained from the CaG-labeled and imaged pre-BötC cells, which are located in superficial layers of the slice, are representative of cells located deeper in the pre-BötC, we performed blind whole-cell patch-clamp recording from multiple inspiratory pre-BötC neurons (in single slices, $n = 15$; 35 neurons total) deeper (100–150 μm) in the slice. Examples of reconstructions of four inspiratory cells (nonintrinsic bursters) labeled with biocytin during whole-cell recording in a single whole-mounted slice are shown in Figure 7. This and all other reconstructions confirmed bilateral axonal projections of pre-BötC neurons with branching axon collaterals in the preMN zone as well as dendritic arborizations extending close to the ventral medullary surface. They also confirmed the basic morphological features (Fig. 8) of soma shapes and size range, primary dendritic branching patterns, and presence of spines on proximal dendrites as found for the CaG-labeled inspiratory neurons.

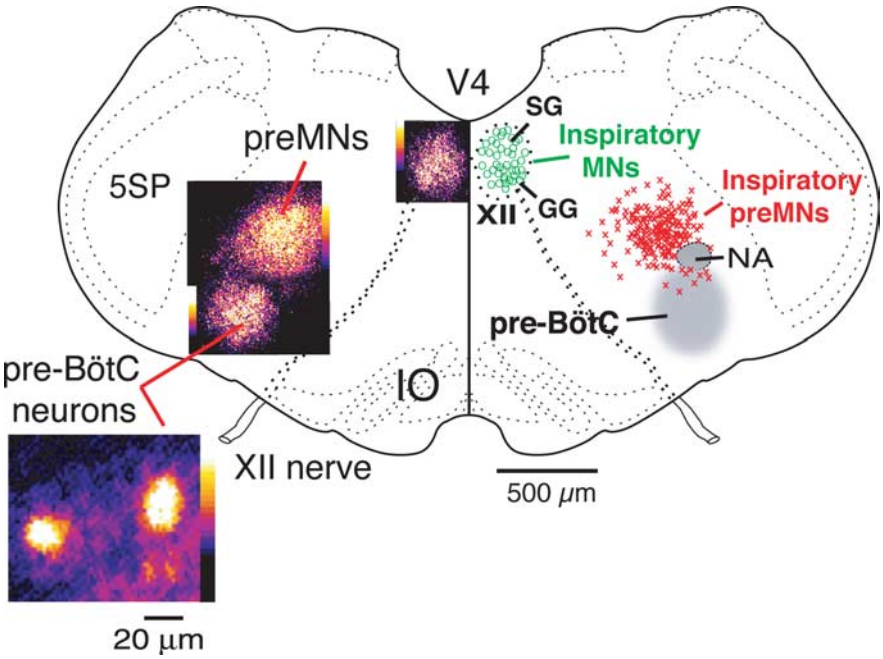

Figure 4. Composite maps of imaged population activity (left) and distributions of single imaged inspiratory XII preMNs and MNs (right) at the medullary level of the *in vitro* slice preparation. Spatial extent and locations of preMNs ($n = 146$; red crosses) are shown in relation to the pre-BötC (gray region at right, population and single-cell CaG fluorescence flash images at left). Distribution of inspiratory XII MNs ($n = 46$; green circles) within the motor nucleus is also shown. Population activity maps (left) were constructed from pseudocolored fluorescence images acquired at 20× magnification and composited from three separate experiments. Maps for the main locus of preMNs obtained by reconstructing the aggregate locations of imaged single neurons (from 40 slices) have a similar location to population activity maps (left) obtained from the lower-magnification population imaging. Within the XII nucleus, there is a bifid distribution with inspiratory cells located in the ventral subdivision of the motor nucleus containing genioglossus (GG) MNs, and a slightly smaller number of inspiratory MNs in the dorsal subdivision, which contains primarily styloglossus (SG) MNs at this level. V4, Fourth ventricle; NA, semicompact division of nucleus ambiguus; 5SP, spinal trigeminal nucleus; IO, inferior olivary nucleus.

PreMNs

Axons of reconstructed preMNs ($n = 12$) projected ipsilaterally (Fig. 6) to the XII motor nucleus and typically exhibited arborizations within the nucleus. We did not detect axonal collateral projections to either the contralateral XII motor nucleus or contralateral preMN region. PreMN dendritic arborizations were mostly confined to the preMN zone mapped by activity imaging. Filling neurons with biocytin during blind patch-clamp recording and subsequent reconstruction of labeled neurons confirmed the presence of XII preMNs in the pre-BötC (4 of 35 neurons identified) (for an example, see Fig. 7) with ipsilateral axonal projections to the XII motor nucleus. All of these neurons were multipolar cells exhibiting variations in soma shape and size (maximal diameters of 15–20 μm) with three to five primary dendrites (Figs. 5–7).

MNs

Reconstructed neurons ($n = 10$) confirmed somata locations in dorsal and ventral motor subnuclei. Axonal projections were within the MN axonal fiber tract coursing ventrally as expected from retrograde labeling of neuron somata via the axon tract or nerve rootlet contained in the slice. Dendritic arborizations, particularly of laterally positioned cells (Figs. 5, 6), extended well beyond the borders of the histologically defined motor nucleus. For reconstructed cells ($n = 2$) (data not shown) located near the most rostral pole of the XII nucleus, dendritic arborizations extended across the midline to the contralateral motor nucleus.

Electrophysiological behavior, synaptic drive, and biophysical properties of inspiratory XII preMNs and MNs

From whole-cell current- and voltage-clamp recordings, we determined intrinsic electrophysiological properties and characteristics of synaptic drive of CaG-labeled inspiratory preMNs and XII MNs. Our analysis of synaptic drive was based on measurements of rhythmic synaptic drive potentials under current clamp and drive currents measured under voltage clamp (holding potential between −70 and −60 mV). Table 1 summarizes biophysical parameters for the preMN and MN populations including whole-cell capacitance (C_m), resting membrane potential, membrane input resistance, and parameters of membrane conductances derived from quasi-steady-state subthreshold current–voltage (I–V) relationships after blocking synaptic drive. Suprathreshold spiking properties including AP shape, repetitive spiking characteristics, and steady-state spiking frequency versus injected current (f–I) relationships were also comparatively analyzed. Note that these properties were measured at elevated extracellular K^+ concentrations (8–9 mM) that are optimal for maintaining rhythmic respiratory network activity in our slice

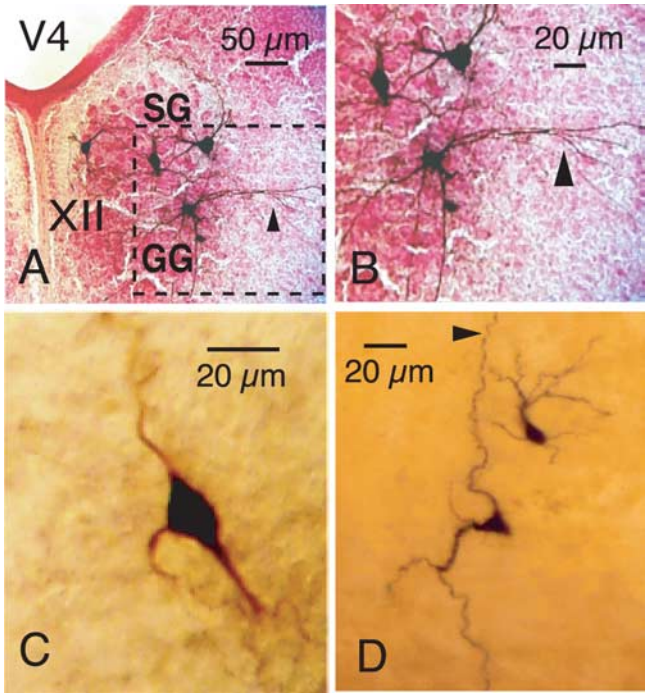

Figure 5. Examples of morphology of inspiratory MNs, preMNs, and pre-BötC neurons identified by CaG fluorescence imaging and subsequently filled with biocytin during whole-cell patch-clamp recording from the CaG-labeled cells. ***A***, Morphology (40× magnification) of four biocytin-filled MNs in a single slice also showing distribution of inspiratory MNs within the XII motor nucleus in styloglossus (SG) and geneoglossis (GG) motoneuron subdivisions of nucleus. ***B***, Enlarged area (dashed box) of the XII nucleus shows motoneuronal somatodendritic morphologies at higher resolution. Stained motoneuron in GG subdivision of nucleus exhibits dendritic projections (arrowheads in ***A*** and ***B***) outside of the nucleus. ***C***, Morphology of XII preMN (enlarged 63× image) showing multipolar distribution of primary dendrites. ***D***, Examples of variations in somatodendritic morphologies (63× magnification, composite image) of labeled pre-BötC inspiratory neurons (both neurons shown exhibited intrinsic bursting properties; see Results for description of different pre-BötC neuron electrophysiological phenotypes). Note axon (arrowhead) of more ventral pre-BötC neuron projecting dorsally toward preMN region. In all images, top is dorsal and bottom is ventral. V4, Fourth ventricle.

preparations. Under these conditions, K^+ currents are reduced (average $E_K = -71$ mV for our recording conditions) relative to those *in vivo*. Accordingly, resting membrane potentials are more depolarized, whereas K^+-dependent afterhyperpolarizations, which affect repetitive spiking behavior and AP shape, are reduced. Comparative analysis of preMN and MN properties is nevertheless possible, because both cell populations were exposed to similar conditions.

Electrophyiological behavior and synaptic drive during rhythmic network activity

Under whole-cell current-clamp recording, all optically identified inspiratory preMNs and MNs exhibited subthreshold rhythmic depolarizing synaptic drive potentials from the resting potential and inspiratory bursts of action potentials (Fig. 9*A*,*B*). The temporal spiking pattern of both preMNs and MNs consisted of a decrementing spike frequency profile (given by spike frequency histograms) (Fig. 9*C*,*D*), which temporally mirrored the declining phase of the synaptic drive potential (Fig. 10). The profile of single MN activity was mirrored by XII MN population activity (Fig. 9*D*), suggesting that the activity pattern at both single-neuron and population levels mostly reflects the temporal patterning of excitatory synaptic drive. Under voltage clamp, preMNs and MNs exhibited similar inward excitatory synaptic drive current envelopes (Fig. 10); these synaptic current waveforms reflected the temporal summation of convergent excitatory synaptic inputs to the cell. The peak inward synaptic currents (I_{syn}) for MNs were almost twice as large as those for preMNs (Fig. 10, Table 1); the synaptic current densities (I_{syn}/C_m), however, were not significantly different (3.8 ± 1.2 pA/pF for preMNs and 3.6 ± 1.3 pA/pF for MNs) (Fig. 10, Table 1). The temporal pattern of the synaptic current envelope (slowly decaying) was closely mirrored by the drive potential envelope and spiking profile of preMNs and MNs (Figs. 9, 10).

Intrinsic electrophysiological behavior

Blockade of non-NMDA glutamatergic synaptic transmission with 20 μM CNQX ($n = 16$ preMNs and 16 MNs in 32 slices total) or blockade of all chemical synaptic transmission by blocking voltage-dependent Ca^{2+} channels with 200 μM Cd^{2+} ($n = 6$ preMNs in six slices) abolished respiratory network activity, eliminated bursting in the inspiratory cells and eliminated rhythmic excitatory synaptic drive currents. Under these conditions, steady depolarizing bias current applied from the resting potential revealed that preMNs and MNs have only two intrinsic electrophysiological states (Fig. 11): quiescence below spiking threshold at membrane potentials including the resting potential, and tonic spiking at suprathreshold potentials. This contrasts with the subpopulation of pre-BötC neurons that generate intrinsic voltage-dependent oscillatory bursting behavior as their baseline membrane potential is shifted over subthreshold voltages between quiescence and tonic spiking, a property that is apparently unique to this subset of pre-BötC cells (Butera et al., 1999a; Koshiya and Smith, 1999; Del Negro et al., 2002).

AP characteristics and repetitive spiking properties

We analyzed repetitive spiking behavior and parameters of AP shape after block of excitatory synaptic transmission (above) for preMNs ($n = 16$) and MNs ($n = 16$). During sustained (2 s) suprathreshold depolarizing steps in applied current from the resting membrane potential (Fig. 11), APs of preMNs and MNs characteristically exhibited a fAHP, ADP, and mAHP (Fig. 11*E*). The durations and amplitudes of the APs as well as these afterpolarizations were not significantly different for the inspiratory preMNs and MNs analyzed (Table 1). With sustained injected suprathreshold current at varying intensities (0.5–1.2 nA), the spike frequency versus time profiles during repetitive spiking in the majority of preMNs and MNs exhibited adaptation [decrementing frequency profile (Fig. 11*C*); 87.5% of preMNs, $n = 14$ of 16; 94% of MNs, $n = 15$ of 16]; the remaining minority of cells exhibited accelerating (augmenting) firing patterns (Fig. 11*C*). PreMNs and MNs exhibited linear steady-state *f–I* relationships (Fig. 11*D*) (average spike frequencies were analyzed after the initial 500 ms of current injection) with similar slopes (31.1 ± 9.7 vs 29.8 ± 10.1 Hz/nA for $n = 6$ preMNs and $n = 6$ MNs, respectively) that were not statistically different ($p > 0.05$) for the subset of cells analyzed.

Subthreshold membrane properties

Subthreshold current–voltage (*I–V*) relationships of a subset of optically identified preMNs ($n = 20$) and MNs ($n = 20$) were obtained from slow voltage-clamp ramps (30 mV/s; −100 to +10 mV). All of these neurons exhibited nonmonotonic, N-shaped *I–V* curves with a linear region spanning membrane voltages below approximately −65 mV, and a negative slope region spanning voltages from approximately −60 to −40 mV (Figs. 12*A*, 13*A*). The linear region represents the combined voltage-insensitive currents (i.e., background or membrane leak current, Leak), with a reversal potential (E_{Leak}) of −65 ± 1.8 mV for

preMNs ($n = 20$) and -63.8 ± 2.1 mV for MNs ($n = 20$), estimated by extrapolation to 0 mV from a linear fit of the *I–V* curve over the voltage range -90 to -65 mV (Figs. 12*A*, 13*A*). These values of E_{Leak} were similar to values of resting membrane potentials obtained from the zero current potential obtained with current-clamp recording in a slightly smaller group of neurons (Table 1). Subtraction of Leak from the total *I–V* curve (Figs. 12*A*,*B*, 13*B*) revealed the subthreshold voltage-activated current components generating the negative slope region, which was primarily attributable to a TTX-sensitive, subthreshold-activating persistent Na^+ current (NaP). Bath-applied TTX (1 μM) blocked most of this subthreshold inward current within 3.6 ± 1.2 min, with a relatively small residual inward current component that persisted after TTX in most cases (Fig. 13*D*), which we assume represents slowly inactivating Ca^{2+} currents; this component was not analyzed further. We extracted the TTX-sensitive NaP component by subtraction of the total *I–V* curves obtained before and after TTX.

We calculated the peak amplitude of NaP (100–240 pA) from the difference in *I–V* relationships, and characterized the voltage dependence of NaP activation by fitting a first-order Boltzmann function to the conductance–voltage data, where the conductance was calculated from the *I–V* relationships and a Na^+ reversal potential of +50 mV (based on bathing and pipette solution Na^+ concentrations). Boltzmann functions fitted to the data yielded a voltage for half-maximal activation $V_{1/2max} = -47.2 \pm 3.2$ and -47.6 ± 3.0 mV for the populations of preMNs and MNs, respectively, and a slope factor $k = 4.9 \pm 0.2$ and 5.0 ± 0.2, respectively (Figs. 12, 13; Table 1). These results showed that the steady-state activation properties of NaP in inspiratory preMNs and MNs were essentially identical. Estimates of NaP maximal conductance (g_{NaP}) indicated that g_{NaP} for MNs was approximately twice that of preMNs (Table 1), whereas NaP conductance densities (g_{NaP}/C_m) were essentially identical for these two neuron populations (Fig. 14). Furthermore, we compared conductance densities for Leak in preMNs and MNs, where g_{Leak} was computed from the linear fits to the *I–V* curves below approximately -65 mV as described above. There was no significant difference between g_{Leak}/C_m of preMNs and MNs (Fig. 14). There was also no significant difference in values of the ratio g_{NaP}/g_{Leak} between these two populations (Table 1).

We also compared NaP and Leak conductances to those of intrinsically bursting ($n = 30$) and nonintrinsically bursting pre-BötC ($n = 20$) inspiratory neurons (Fig. 14) from the data set previously reported by Purvis et al. (2007) (conductance values here normalized to C_m). This data set was obtained by measurement protocols identical to those used for preMNs and MNs; Boltzmann functions for steady-state activation of NaP in the pre-BötC neurons were essentially identical with those for preMNs and MNs, and Leak reversal potentials were also nearly identical. NaP conductance densities (g_{NaP}/C_m) were significantly higher in pre-BötC intrinsic bursting neurons, as predicted

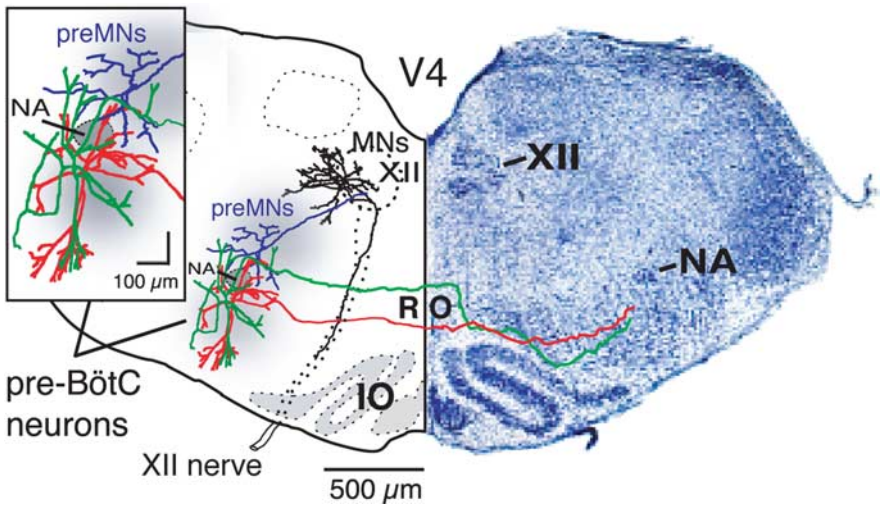

Figure 6. Examples of morphological reconstructions of inspiratory pre-BötC neurons, XII preMNs and MNs illustrating spatial arrangement of dendritic trees and axonal projections in relationship to loci (gray areas) of neuronal somata and population activity mapped by CaG imaging. Dendritic trees of pre-BötC neurons (green, red) extend beyond region of mapped somata toward ventral medullary surface and dorsally into preMN region; axons project across midline through the nucleus raphé obscurus (RO) to contralateral pre-BötC with (green) or without (red) traversing through preMN region. The pre-BötC neuron shown in red exhibited intrinsic bursting properties, whereas the green neuron did not. PreMN (blue) dendritic trees are more compact and mostly confined to region of preMN somata; axon projects ipsilaterally to XII motor nucleus. Regions of pre-BötC neuron and preMN somata are separated by semicompact division of nucleus ambiguus (NA) containing cranial MNs. Dendritic trees of many inspiratory XII MNs (black) extend outside of motor nucleus; axons project ipsilaterally within ventrally traversing nerve fiber tract. Cytoarchitectonic appearance (cresyl violet-stained section) of medulla at level of the reconstructions within the *in vitro* slice preparation is shown for reference (right side).

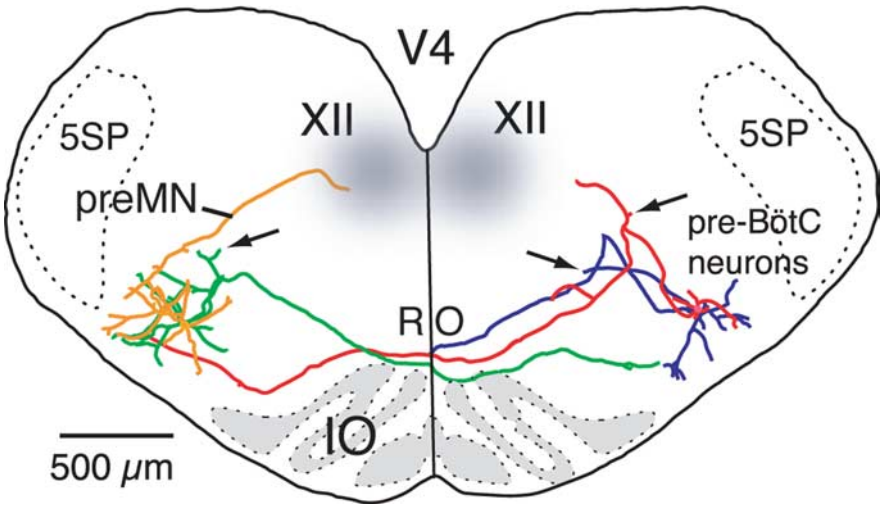

Figure 7. Patterns of axonal projections and cell morphology of pre-BötC inspiratory cells (nonintrinsic bursters shown) as reconstructed from biocytin-filled neurons recorded by blind whole-cell recording of multiple inspiratory neurons bilaterally in the same slice. Neurons were located 100–150 μm below the slice surface. Two cells (green, red) show axonal projections across the midline at the level of nucleus raphé obscurus (RO) immediately dorsal to the inferior olivary (IO) nucleus and continuing into ventral dendritic zones of contralateral pre-BötC neurons. The axon of the other neuron (blue) exited the slice after crossing the midline. The arrows point to axon collateral arborizations of three cells in the preMN zone. Reconstructed pre-BötC preMN (yellow) has ipsilateral projection to the XII motor nucleus. 5SP, Spinal trigeminal nucleus.

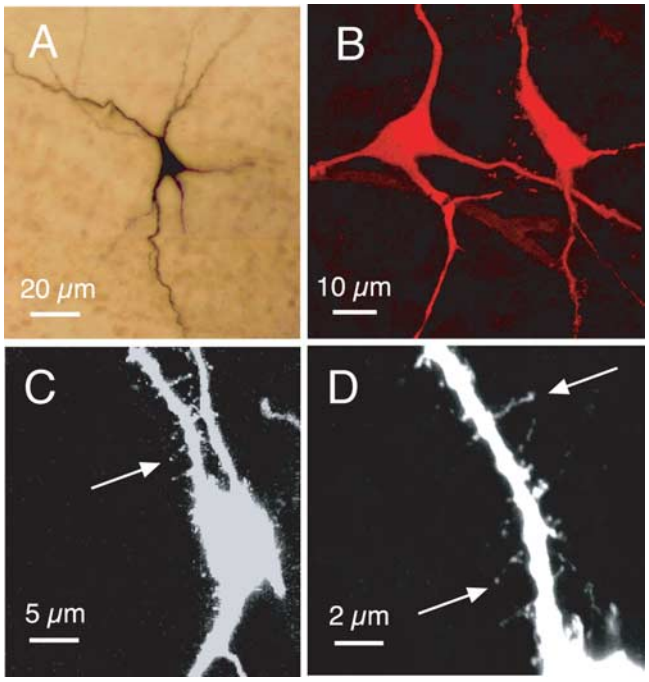

Figure 8. Morphological features of somata and primary dendrites of pre-BötC inspiratory neurons. ***A***, Light microscopic image (composited from multiple merged 20× magnification photomicrographs) of intrinsic burster inspiratory neuron *in situ* in whole-mounted fixed slice preparation. ***B***, Confocal image of two nonintrinsically bursting pre-BötC neurons labeled with Texas Red (100×; two-dimensional projection from merged image stack; 615 nm emission wavelength). ***C***, ***D***, Confocal images (63× magnification in ***C***; 100× in ***D***) of Texas Red-labeled nonintrinsically bursting pre-BötC inspiratory neuron, showing examples of spines on primary dendrites. Image in ***C***, showing several primary dendrites, is a two-dimensional projection from the merged image stack. Higher-magnification image in ***D*** is focused on a single primary dendrite of the cell shown in ***C*** (note that the medial dendrite in ***C*** is out of the focal plane and therefore does not appear in the image shown in ***D***). Original color projection images have been inverted into black-and-white for clearer resolution of dendritic spines.

Table 1. Summary of biophysical/electrophysiological parameters for populations of inspiratory XII preMNs and MNs

Parameter	XII preMNs	XII MNs
Resting membrane potential (mV)	−59.2 ± 4.8	−62.4 ± 4.6
Action potential amplitude (mV)	88.6 ± 6.4	89.2 ± 5.8
Action potential duration (ms)	1.42 ± 0.12	1.44 ± 0.16
mAHP amplitude (mV)	4.2 ± 2.0	4.8 ± 2.4
mAHP duration (ms)	90.0 ± 29.0	99.0 ± 36.0
mAHP half-duration (ms)	31.6 ± 9.4	35.2 ± 10.2
C_m (pF)[a]	32.1 ± 2.3	63.4 ± 2.1*
g_{NaP} (nS)[a]	1.26 ± 0.34	2.52 ± 0.60*
NaP g/g_{max}:$V_{1/2max}$ (mV)[a]	−47.2 ± 3.2	−47.6 ± 3.0
Boltzmann slope factor (k)[a]	4.9 ± 0.2	5.0 ± 0.2
g_{Leak} (nS)[a]	4.14 ± 1.57	9.36 ± 3.00*
R_m (MΩ)	227.0 ± 63.7	107.1 ± 33.0*
Ratio: g_{NaP}/g_{Leak}[a]	0.33 ± 0.10	0.29 ± 0.09
Peak synaptic current I_{syn} (pA)	122.0 ± 39.0	229.0 ± 87.0*
I_{syn}/C_m (pA/pF)	3.81 ± 1.21	3.61 ± 1.37

Values represent means ± SD.

For populations of XII preMNs, $n = 16$ or [a]20, and for XII MNs, $n = 16$ or [a]20.

*$p < 0.01$, parameters were significantly different. All other parameters were not statistically different ($p > 0.05$) between preMNs and MNs.

by our theory for NaP-dependent bursting (Butera et al., 1999a,b; Del Negro et al., 2002; Purvis et al., 2007), whereas g_{Leak} densities of intrinsically bursting and nonintrinsically bursting neurons were not significantly different. Except for pre-BötC intrinsic bursters, all other neurons had nonstatistically different densities for either g_{NaP} or g_{Leak}. Thus, g_{NaP} density distinguishes the subpopulation of intrinsic bursters from all other circuit neurons within and outside the pre-BötC. The possible significance of high g_{NaP} densities in subpopulations of pre-BötC neurons for inspiratory rhythm generation in the pre-BötC has been discussed extensively previously (Butera et al., 1999a,b; Purvis et al., 2007).

Discussion

The architecture and functional characteristics of brainstem respiratory circuits are not well established. We reconstructed several structural features of the neonatal rat pre-BötC–XII preMN–MN circuit: (1) many preMNs are segregated from rhythm-generating pre-BötC neurons, an architectonic arrangement found for bulbospinal circuits (Smith et al., 1991; Feldman and Smith, 1995; Guyenet et al., 2002; Stornetta et al., 2003a,b), which, *in vivo*, may facilitate downstream integration of inputs for premotor pattern formation; and (2) circuit connections, which we infer from axonal projection and arborization patterns, are contralateral for interneurons at the level of pre-BötC, but mainly ipsilateral downstream from preMNs to MNs. We emphasize that these projection patterns represent those confined to the level of our slices (i.e., at the level of pre-BötC and rostral XII motor nucleus). Furthermore, we only identified projections of a subset of preMNs and pre-BötC cells; neurons with connections exclusively outside of the slice are not labeled by our functional neural tracing approach. Our functional analysis suggests that XII preMNs and MNs have a number of similar electrophysiological and synaptic integration properties, which we hypothesize reflects biophysical and synaptic specialization common to neurons transmitting rhythmic drive in this circuit.

Topographic organization of rhythm generation and drive transmission circuits

Locus of pre-BötC activity

Our imaging approach defined loci of interneurons with axonal cross-connections. This population, which represents a subset of the total pre-BötC population, maps to the locus of rhythmically active neurons defined electrophysiologically *in vitro* (Funk et al., 1993; Lieske et al., 2000) and *in vivo* (Schwarzacher et al., 1995), by previous functional neurotracing *in vitro* (Koshiya and Smith, 1999), and where perturbations of neuronal excitability or neuronal ablations disturb inspiratory rhythm generation (Koshiya and Guyenet, 1996; Gray et al., 2001). Axonal projections and somatodendritic morphology of pre-BötC neurons have not been established in detail previously. We show the following: (1) contralateral axonal projections that we suggest reflect interconnections synchronizing pre-BötC activity; (2) axon collateral projections within the preMN zone, potentially transmitting rhythmic drive; and (3) distal dendritic arborizations extending near the ventral medullary surface that likely represent synaptic integration sites. Thus, an important implication is that the functional extent of the pre-BötC defined by somatodendritic architecture encompasses a much larger reticular formation region than defined

solely by cell body locations. We note that we have not yet established functionally or morphologically, at the level of synapses/synaptic interactions, direct connections between single, contralateral pre-BötC neurons or between single pre-BötC cells and labeled preMNS. Additional electrophysiological and morphological analyses will be required to definitively establish such connections.

Locus of preMNs

Locations of XII preMNs investigated by transynaptic tracing methods (Dobbins and Feldman, 1995) in adult rats, similar to our results, show reticular formation cells diffusely distributed between the motor nucleus and NA, although these cells were previously not identified as respiratory-modulated neurons. Studies of a small number of respiratory preMNs suggested a similar distribution (Peever et al., 2002). We visualized inspiratory preMNs at the level of our slices. PreMNs were clustered within a locus bounded ventrally by nucleus ambiguous semicompact formation and the lateral paragigantocellular reticular nucleus, and dorsolaterally by the parvicellular reticular nucleus. Axonal projections to rostral MNs are primarily ipsilateral, with some, but relatively few, inspiratory preMNs within the pre-BötC (Dobbins and Feldman, 1995; Peever et al., 2002). Dendritic arborizations appear confined to the zone of preMN somata, suggesting local dendritic synaptic input connections. However, many dendrites may have been cut at the surface of our slices, so additional study of preMN dendritic architecture is required. We also identified preMN axon collaterals within this area, suggesting local synaptic interactions.

We found a smaller subset of preMNs within the pre-BötC; a subpopulation of bulbospinal preMNs has also been identified in neonatal rats (Ellenberger, 1999). This implies a potentially complex spatial distribution of premotor and propriobulbar interneurons within the pre-BötC that begs additional study.

Myotopic organization of inspiratory XII MNs

Innervation of tongue muscles by respiratory motoneurons is important for coordinating upper airway muscles with respiratory movements and maintenance of a patent upper airway (Bartlett et al. 1990). We find inspiratory neurons distributed within ventral and dorsal subdivisions of the XII nucleus at the level of our slices. The ventral subdivision contains primarily MNs innervating the extrinsic protrussor

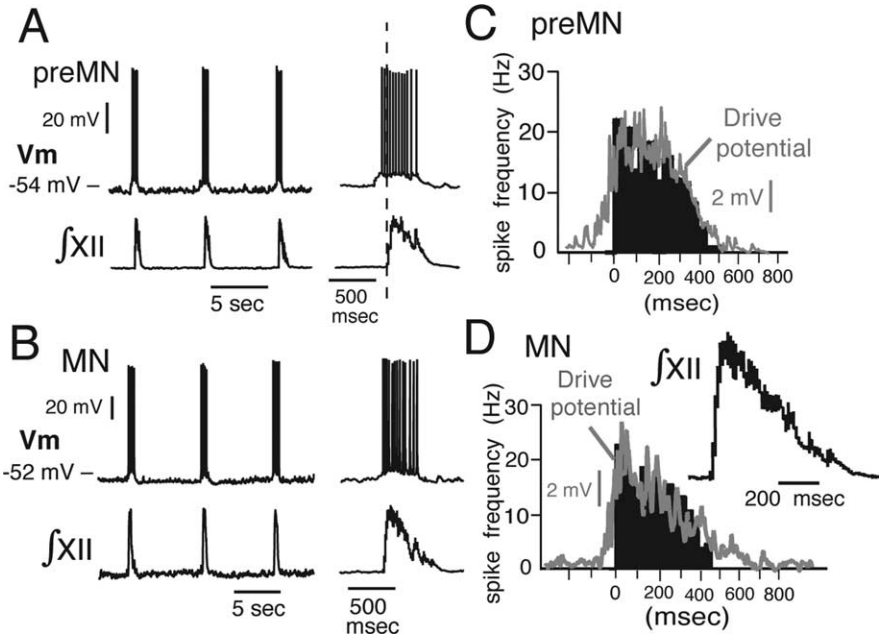

Figure 9. Representative rhythmic bursting behavior of imaged XII preMNs and MNs. ***A***, ***B***, Examples of whole-cell current-clamp recordings (V_m) of synaptically driven rhythmic bursting of preMN (***A***) and MN (***B***) during network inspiratory activity monitored by XII motor output (∫XII). ***C***, ***D***, Histograms (black; average of 15 cycle-triggered bursts) show examples of spike frequency profiles of preMNs (***C***) and MNs (***D***) during inspiratory bursts. Rapidly peaking-declining spike frequency profile follows the time course of synaptic drive potentials shown by gray traces superimposed on histograms. Temporal profile of single MN spiking activity is mirrored by XII MN population activity (∫XII, average of 15 integrated population discharges shown at right in ***D***). Spiking pattern of preMNs is similar to MNs, but onset of spiking during inspiratory bursts, although variable from cycle to cycle, in some preMNs occurred before generation of MN population activity (for example, see vertical dashed line in ***A***), reflecting earlier onset of synaptic drive (for detailed examples of synaptic drive potentials and currents, see Fig. 10).

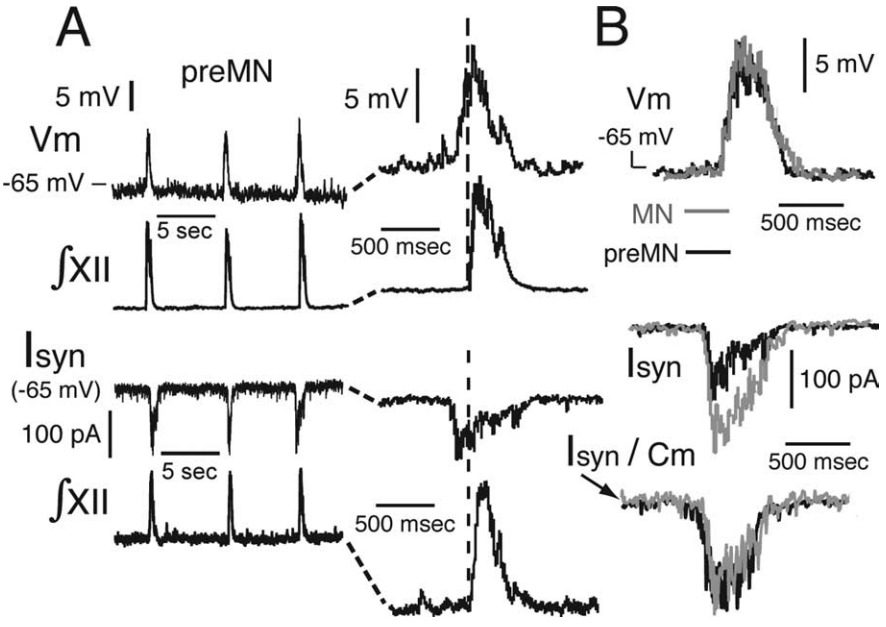

Figure 10. Temporal characteristics of rhythmic synaptic drive in XII preMNs and MNs. ***A***, Inspiratory synaptic drive potentials (V_m) in a representative preMN measured under current clamp (top) and excitatory drive currents (I_{syn}) measured under voltage clamp (bottom) in another representative preMN. The time course of drive potentials were revealed by applying hyperpolarizing current to maintain neuron at subthreshold voltages to prevent spiking. Expanded time base for V_m and I_{syn} is shown at right. Waveforms of synaptic potentials and currents reflect temporal summation of rhythmic excitatory inputs. Development of drive at preMN level begins ~100–200 ms before generation of MN population activity (∫XII) downstream (see vertical dashed line). ***B***, Comparison of subthreshold drive potential waveforms for preMN (black) and MN (gray trace superimposed; average of 10 cycles each; onset timing differences removed), showing similar amplitudes and time courses. Synaptic currents of MNs are typically almost twice as large as preMN currents (Table 1). Currents normalized to whole-cell capacitance (I_{syn}/C_m) are nearly identical (bottom right).

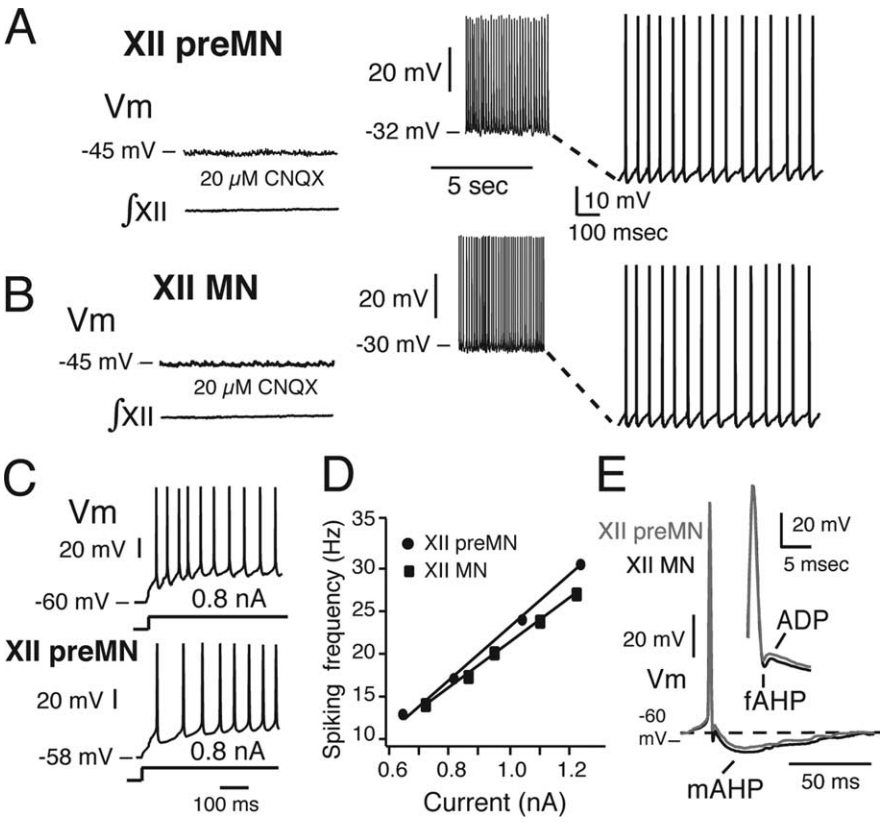

Figure 11. Repetitive spiking properties of inspiratory XII preMNs and MNs. ***A***, ***B***, After block of rhythmic non-NMDA glutamatergic receptor-mediated excitatory synaptic transmission (with 20 μM CNQX), progressive depolarization of preMN (***A***) and MN (***B***) V_m from resting state by applied current in current clamp shows silence below and repetitive spiking above AP generation threshold. ***C***, Example of adapting/decrementing firing pattern characteristic of the majority (87%) of preMNs (and MNs, not shown) during sustained depolarization after a step in applied current (0.8 nA) from resting state; incrementing pattern exhibited by a minority of preMNs (and MNs) is also shown. ***D***, Representative linear *f–I* relationships for an inspiratory preMN and MNs (see Materials and Methods for comparisons of *f–I* slopes for groups of preMNs and MNs). ***E***, Temporal characteristics of APs of XII inspiratory preMNs and MNs. The AP time courses are shown, including interspike interval during repetitive spiking, of preMN (gray) and MN (black), illustrating fAHP, ADP, and mAHP (see Materials and Methods for definitions).

genioglossus muscle with intrinsic tongue muscle MNs distributed more medially (Berger and Bellingham, 1995; McClung and Goldberg, 2002). The dorsal subdivision contains MNs innervating extrinsic retractor (styloglossus and hyoglossus) muscles. In general, our results show inspiratory MNs in zones containing genioglossus, styloglossus, hyoglossus, and intrinsic MNs, a subnuclear organization reflecting myotopic innervation patterns of respiratory-modulated tongue muscles (Bailey and Fregosi, 2004). Dendritic arborizations of some inspiratory MNs extended beyond the border of XII (Berger and Bellingham, 1995), an arrangement again implying synaptic connections/integration outside the cell body nucleus.

Electrophysiological properties of XII MNs and preMNs

AP shapes and repetitive spiking properties

Electrophysiological properties of inspiratory XII preMNs have not been analyzed previously. Properties and APs of neonatal and adult rat hypoglossal motoneurons have been extensively analyzed (Viana et al., 1995; Sawezuk et al., 1997; Powers and Binder, 2003). However, in these previous studies, MNs examined were not identified respiratory cells, which represent a subset of the heterogeneous XII MN population. Our results, consistent with these previous studies, show that (1) the majority of inspiratory MNs, regardless of location, exhibited spike frequency adaptation; (2) steady-state *f–I* relationships were linear with similar gains (~30 Hz/nA); and (3) all neurons exhibited ADPs and prominent mAHPs, with amplitudes similar to previously reported values (Viana et al., 1995). AP and mAHP durations of respiratory cells fall within reported dynamic ranges for neonatal MNs, longer than adult MNs in which shortening of AP and mAHP durations are a prominent developmental change (Viana et al., 1995).

According to modeling studies (Purvis and Butera, 2005), XII MN AP shape, including afterpolarizations, can be explained by dynamic interactions of a palette of intrinsic currents identified in rat XII (and other) MNs. These include voltage-dependent persistent Na^+ (NaP) and Ca^{2+} currents (N-, P-, and L-type), I_H, I_A, and Ca^{2+}-activated K^+ conductances (SK, BK). We have not studied these conductances (except NaP); the similar AP shapes, afterpolarizations, and repetitive spiking properties between the inspiratory cells and these previously studied MNs suggest a similar set of currents. We conclude that suprathreshold properties of inspiratory MNs are similar to the majority of neonatal XII MNs. Furthermore, conductance-based models for generic neonatal XII MNs may apply to both inspiratory MNs and preMNs (when current densities are normalized for differences in neuronal size). We note, however, that whereas subthreshold conductance densities on average were similar in pre-MNs and MNs, there is heterogeneity (e.g., g_{Leak} densities varied by a factor of 3–4 in each population). Similarly, many different combinations of conductance densities within the set of suprathreshold currents could theoretically produce the same dynamic behavior in terms of AP waveforms and spiking properties (Schulz et al., 2006).

Functional significance of NaP and Leak in preMNs and MNs

Voltage-activated persistent currents including NaP are thought to amplify depolarizing synaptic drive during conversion into repetitive discharge. NaP is the major persistent current in MNs and preMNs activated initially during subthreshold depolarization from resting potentials. The NaP that we measured had identical activation properties and conductance densities in MNs and preMNs. Furthermore, we did not observe other major subthreshold persistent inward currents (i.e., at voltages less than −40 mV in which there was a relatively small TTX-resistant residual inward current), consistent with observations that the largest Ca^{2+} current components (N-, P-, and secondarily L-type) in XII MNs activate at more depolarized voltages (Powers and Binder, 2003). Thus, NaP activation may serve to initially amplify subthreshold rhythmic synaptic drive and facilitate drive transmission; NaP in general has been postulated to contribute to neuronal excitability and amplification of subthreshold oscillations (Crill, 1996; Vervaeke et al., 2006). NaP inactivation during synaptic drive on the timescale of the inspiratory burst (500–700

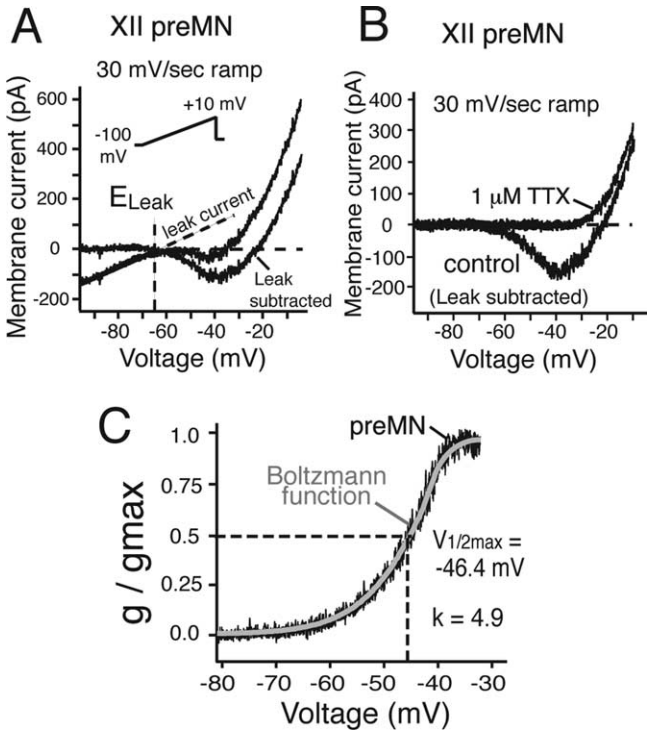

Figure 12. Whole-cell *I–V* relationships of inspiratory XII preMNs. ***A***, *I–V* relationships obtained from 30 mV/s voltage-clamp ramps (−100 to +10 mV; inset) for preMN before and after subtraction of Leak, obtained by linear fit of the *I–V* curve at hyperpolarized voltages (less than −65 mV). Leak reversal potential (E_{Leak}, −65 mV) is indicated. ***B***, TTX eliminates major inward current component (TTX-sensitive NaP) in the Leak-subtracted *I–V* relationships between −60 and −30 mV. ***C***, Plots of NaP g/g_{max} versus voltage for preMN (black) with superimposed first-order Boltzmann function fit (gray curve), indicating quasi-steady-state, voltage-dependent activation characteristics for NaP with half-maximal activation voltage ($V_{1/2max}$) and slope factor *k*.

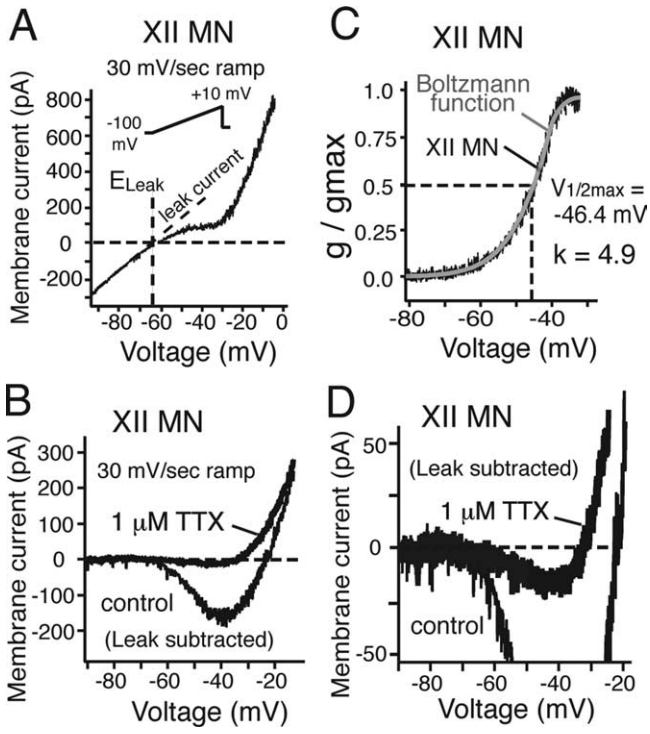

Figure 13. Whole-cell *I–V* relationships of inspiratory XII MNs. ***A***, ***B***, *I–V* relationships obtained from 30 mV/s voltage-clamp ramps (−100 to +10 mV; inset) for MN before (***A***) and after (***B***) subtraction of Leak, obtained by linear fit of the *I–V* curve at hyperpolarized voltages (less than −65 mV). Leak reversal potential (E_{Leak}, −64 mV) is indicated. TTX eliminates major inward current component (TTX-sensitive NaP) in the Leak-subtracted *I–V* relationships (***B***) between −60 and −30 mV. ***C***, Plots of NaP g/g_{max} versus voltage for both MN (black) with superimposed first-order Boltzmann function fit (gray curve) with half-maximal activation voltage ($V_{1/2max}$) and slope factor *k* indicated. ***D***, Expanded current scale for MN shown in ***B*** indicates small (<25 pA) residual TTX-insensitive subthreshold inward current.

ms) may affect both transient (Vervaeke et al., 2006) and steady-state (Purvis and Butera, 2005) *f–I* gain.

Leak is dominated by K^+ current with similar conductance densities in preMNs and MNs. In contrast to the pre-BötC subpopulation with intrinsic bursting properties where g_{NaP} is larger in relation to g_{Leak}, in preMNs and MNs g_{Leak} is larger than g_{NaP} by a factor of ~3 (Table 1). Thus, Leak is a major determinant of preMN/MN excitability. TASK channels contribute to Leak at least in XII MNs (Talley et al., 2000; Bayliss et al., 2003); modulation of Leak via these channels (Talley et al., 2000) may provide a fundamental mechanism for excitability control.

Synaptic drive waveforms, preMN/MN spiking patterns, and fidelity of excitatory drive in vitro

Although inspiratory preMNs and MNs may have a complex set of currents, our analysis indicates that spiking profiles during inspiratory bursts mostly reflect the waveform and convergence of rhythmic synaptic drive. This excitatory waveform originates in the pre-BötC (Butera et al. 1999b; Del Negro et al., 2001) and propagates, according to our data, with high fidelity. Despite marked differences in preMN and MN size/somatodendritic morphology, synaptic conductance/current densities are similar. Furthermore, the similar g_{NaP} or g_{Leak} densities imply similar contributions of these currents to neuronal responses to depolarizing synaptic drive.

We conclude that neuronal and synaptic properties are such that the strength of excitatory drive is conserved across this circuit and there is similar integration/conversion of synaptic input

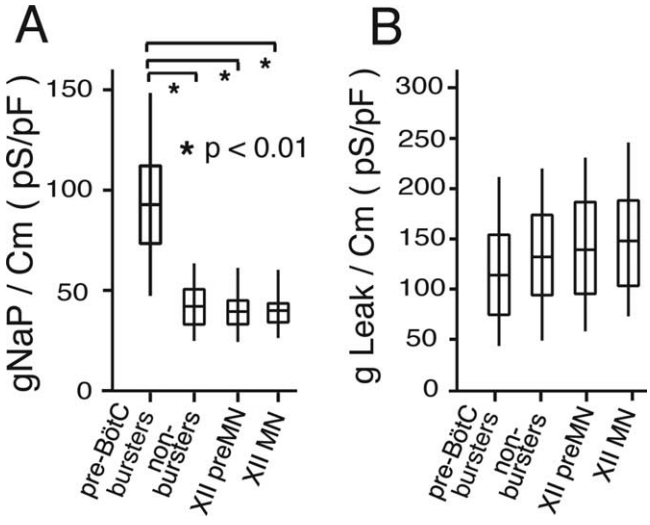

Figure 14. Comparative summary of g_{NaP} and g_{Leak} densities for different populations of inspiratory neurons in the pre-BötC–preMN–MN circuit *in vitro*. ***A***, ***B***, Box plots showing distributions of g_{NaP} and g_{Leak}, normalized to cell capacitance (C_m) for inspiratory XII preMNs ($n = 20$), MNs ($n = 20$), and the two different types of pre-BötC inspiratory neurons, intrinsically bursting ($n = 30$; labeled as pre-BötC bursters) and nonintrinsically bursting ($n = 20$; labeled as nonbursters). Mean values of g_{Leak}/C_m are statistically identical ($p > 0.05$) for the different cell populations, whereas mean g_{NaP}/C_m values are statistically higher (one-way factorial parametric ANOVA) for pre-BötC bursting cells. The middle line of the box plots represents the median, the box itself spans ±0.67 times the SD [quartiles 1–3 or the interquartile range (IQR)], and the "whiskers" above and below the box are quartile 3 +1.5 times the IQR and quartile 1 −1.5 times the IQR, respectively.

into neuronal spiking output at preMN and MN levels of the circuit. This concept may apply to other respiratory transmission circuits, but comparative electrophysiological studies have not been conducted. Additional investigation is required to test the functional principles postulated here for the pre-BötC–hypoglossal preMN–MN transmission circuit.

References

Bailey EF, Fregosi RF (2004) Coordination of intrinsic and extrinsic tongue muscles during spontaneous breathing in rat. J Appl Physiol 96:440–449.

Bartlett Jr D, Leiter JC, Knuth SL (1990) Control and actions of the genioglossus muscle. Prog Clin Biol Res 345:99–107.

Bayliss DA, Sirois JE, Talley EM (2003) The TASK family: two-pore domain background K^+ channels. Mol Interv 3:205–219.

Berger A, Bellingham M (1995) Determinants of respiratory motor output. In: Regulation of breathing (Dempsey JA, Pack AI, eds), pp 39–69. New York: Dekker.

Butera RJ, Rinzel J, Smith JC (1999a) Models of respiratory rhythm generation in the pre-Bötzinger complex. I. Bursting pacemaker neurons. J Neurophysiol 82:382–397.

Butera RJ, Rinzel J, Smith JC (1999b) Models of respiratory rhythm generation in the pre-Bötzinger complex. II. Populations of coupled pacemaker neurons. J Neurophysiol 82:398–415.

Crill WE (1996) Persistent sodium current in mammalian central neurons. Annu Rev Physiol 58:349–362.

Del Negro CA, Johnson SM, Butera RJ, Smith JC (2001) Models of respiratory rhythm generation in the pre-Bötzinger complex. III. Experimental tests of model predictions. J Neurophysiol 86:59–74.

Del Negro CA, Koshiya N, Butera RJ, Smith JC (2002) Persistent sodium current, membrane properties, and bursting behavior of pre-Bötzinger complex inspiratory neurons in vitro. J Neurophysiol 88:2242–2250.

Dobbins EG, Feldman JL (1995) Differential innervation of protruder and retractor tongue muscles of rat. J Comp Neurol 357:376–394.

Dödt HU, Zieglgänsberger W (1994) Infrared videomicroscopy: a new look at neuronal structure and function. Trends Neurosci 17:453–458.

Ellenberger HH (1999) Nucleus ambiguus and bulbospinal ventral respiratory group neurons in the neonatal rat. Brain Res Bull 50:1–13.

Feldman JL, Smith JC (1995) Neural control of respiratory pattern in mammals: an overview. In: Regulation of breathing (Dempsey JA, Pack AI, eds), pp 39–69. New York: Dekker.

Feldman JL, Smith JC, McCrimmon, DR, Ellenberger HH, Speck DF (1988) Generation of respiratory pattern in mammals. In: The neural control of rhythmic movements in vertebrates (Cohen AM, Grillner S, Rossignol S, eds), pp 73–100. New York: Wiley.

Fetcho JR, O'Malley DM (1995) Visualization of active neural circuitry in the spinal cord of intact zebrafish. J Neurophysiol 73:399–406.

Foskett JK (1988) Simultaneous nomarski and fluorescence imaging during videomicroscopy of cells. Am J Physiol 255:C566–C571.

Funk G, Smith JC, Feldman JL (1993) Generation and transmission of respiratory oscillations in medullary slices: role of excitatory amino acids. J Neurophysiol 70:1497–1515.

Gray PA, Janczewski WA, Mellen N, McCrimmon DR, Feldman JL (2001) Normal breathing requires preBötzinger complex neurokinin-1 receptor-expressing neurons. Nat Neurosci 4:927–930.

Grillner S, Markram H, DeSchutter E, Silberberg G, LeBeau FEN (2005) Microcircuits in action—from CPGs to neocortex. Trends Neurosci 28:525–533.

Guyenet PG, Sevigny CP, Weston MC, Stornetta RL (2002) Neurokinin-1 receptor-expressing cells of the ventral respiratory group are functionally heterogeneous and predominantly glutamatergic. J Neurosci 22:3806–3816.

Horikawa K, Armstrong WE (1988) A versatile means of intracellular labeling: injection of biocytin and its detection with avidin conjugates. J Neurosci Methods 25:1–11.

Koshiya N, Guyenet PG (1996) Tonic sympathetic chemoreflex after blockade of respiratory rhythmogenesis in the rat. J Physiol (Lond) 491:859–869.

Koshiya N, Smith JC (1999) Neuronal pacemaker for breathing visualized in vitro. Nature 400:360–363.

Lieske SP, Thoby-Brisson M, Telgkamp P, Ramirez JM (2000) Reconfiguration of the neural network controlling multiple breathing patterns: eupneas, sighs, and gasps. Nat Neurosci 3:600–607.

McClung JR, Goldberg SJ (2002) Organization of the hypoglossal motoneurons that innervate the horizontal and oblique components of the genioglossus muscle in the rat. Brain Res 950:321–324.

O'Donovan M, Ho S, Yee W (1994) Calcium imaging of rhythmic network activity in the developing spinal cord of the chick embryo. J Neurosci 14:6354–6369.

Peever JH, Shen L, Duffin J (2002) Respiratory pre-motor control of hypoglossal motoneurons in the rat. Neurosci 110:711–722.

Powers RK, Binder M (2003) (2003) Persistent sodium and calcium currents in rat hypoglossal motoneurons. J Neurophysiol 89:615–624.

Purvis LK, Butera RJ (2005) Ionic current model of a hypoglossal motoneuron. J Neurophysiol 93:723–733.

Purvis LK, Smith JC, Koizumi H, Butera RJ (2007) Intrinsic bursters increase the robustness of rhythm generation in an excitatory network. J Neurophysiol 97:1515–1526.

Rekling JC, Feldman JL (1998) PreBötzinger complex and pacemaker neurons: hypothesized site and kernel for respiratory rhythm generation. Annu Rev Physiol 60:385–405.

Sawezuk A, Poweres RK, Binder MD (1997) Contribution of outward currents to spike frequency adaptation in hypoglossal motoneurons of the rat. J Neurophysiol 78:2246–2253.

Schulz D, Goaillard J-M, Marder E (2006) Variable channel expression in identified single and electrically coupled neurons in different animals. Nat Neurosci 9:356–362.

Schwarzacher S, Smith JC, Richter DW (1995) The pre-Bötzinger complex in the cat. J Neurophysiol 73:1452–1461.

Smith JC, Ellenberger HH, Ballanyi K, Richter DW, Feldman JL (1991) Pre-Bötzinger complex: a brainstem region that may generate respiratory rhythm in mammals. Science 254:726–729.

Stornetta RL, Sevigny CP, Guyenet PG (2003a) Inspiratory augmenting bulbospinal neurons express both glutamatergic and enkephalinergic phenotypes. J Comp Neurol 455:113–124.

Stornetta RL, Rosin DL, Wang H, Sevigny CP, Weston MC, Guyenet PG (2003b) A group of glutamatergic interneurons expressing high levels of both neurokinin-1 receptors and somatostatin identifies the region of the pre-Bötzinger complex. J Comp Neurol 455:499–512.

Talley EM, Lei Q, Sirios JE, Bayliss DA (2000) TASK-1, a two-pore domain K^+ channel is modulated by multiple neurotransmitters in motoneurons. Neuron 25:399–410.

Vervaeke K, Hu H, Grahm LJ, Storm JF (2006) Contrasting effects of the persistent Na^+ current on neuronal excitability and spike timing. Neuron 49:257–270.

Viana F, Bayliss DA, Berger AJ (1995) Repetitive firing properties of developing rat brainstem motoneurones. J Physiol (Lond) 486:745–761.